



Numerical analysis of added resistance on ships in short waves

Min-Guk Seo, Kyung-Kyu Yang, Dong-Min Park, Yonghwan Kim

Show more

Outline Share Cite

<https://doi.org/10.1016/j.oceaneng.2014.05.011>

[Get rights and content](#)

Highlights

- Numerical analysis has been focused on added resistance in short waves.
- To improve the accuracy of added resistance prediction, grid convergence test should be performed.
- Three-dimensional method is recommended in short waves.
- Linear solution with fine solution meshes can provide good results, but nonlinear theory is preferred in slender hulls.

Abstract

In the present study, a Rankine panel method, which is based on the potential theory and a Cartesian-grid method, which solves the Euler equation directly, are applied to calculate ship motion and added resistance. In the Rankine panel method, a near-field method which calculates added resistance by integrating the second-order pressure on a body surface is adopted. In the Cartesian grid method, the wave–body interaction problem is considered as a multiphase problem, and volume fraction functions are defined in order to distinguish each phase in a Cartesian grid system. The added resistance is calculated by subtracting the steady surge force from the mean surge force measured in motion problems. This study focuses on added resistance under short wave conditions. Calculation capacities of the Rankine panel method and Cartesian grid method in short wavelength are systematically analyzed for several models, including Series 60 hulls ($C_F=0.7, 0.8$), S175 containerhips and KVLCC2 hulls. In addition, established asymptotic methods in short wavelength are examined.

Previous

Next

Keywords

Added resistance; EEDI; Short wave approximation; Rankine panel method; Cartesian grid method; Grid convergence test

1. Introduction

Traditionally, ship resistance problems have been considered in still water conditions. Ocean-going vessels, however, often meet sea conditions which influence ship resistance and propulsion efficiency, and ship's forward speed decreases compared to that in calm sea conditions, because of added resistance. It is reported that the magnitude of added resistance is about 15–30% of calm-water resistance. An accurate prediction of this added resistance, therefore, is important in prescribing an appropriate propulsion power to a ship. Moreover, in recent years, the International Maritime Organization (IMO) has made regulations relating to the measurement of energy efficiency level such as Energy Efficiency Design Index (EEDI) to restrict green-house gas emissions from ships. For these reasons, ship designers should find optimum hull forms to minimize resistance in ocean waves, and pay more attention to added resistance problem.

Added resistance due to waves is one of the major components affecting ship performance. Since 1970s the added resistance problem due to waves has been widely studied by conducting experiments, and several results have been introduced into this field. [Gerritsma and Beukelman \(1972\)](#) showed that added resistance varies linearly, as the square of wave height and the influence of surge motion on added resistance may be negligible. [Storm-Tejse et al. \(1973\)](#) measured added resistance on a destroyer, a high-speed displacement hull and the five Series 60 parent hulls. Added resistances on a S175 containerhip were measured by [Fujii and Takahashi \(1975\)](#) and [Nakamura and Naito \(1977\)](#). Also, added resistances on Wigley hull forms were measured by [Journée \(1992\)](#). [Guo and Steen \(2011\)](#), [Sadat-Hosseini et al. \(2013\)](#) and [Lee et al. \(2013\)](#) studied added resistance on KVLCC2 model hulls.

Meanwhile, there are two major numerical approaches which can be used to analyze the added resistance problem: the far-field and near-field methods. The far-field method, which is based on the momentum conservation theory, was introduced by [Maruo \(1960\)](#). It was further elaborated by [Newman \(1967\)](#), [Gerritsma and Beukelman \(1972\)](#) and [Salvesen \(1978\)](#). Recently, [Kashiwagi et al. \(2009\)](#) used Maruo's approach to calculate added resistance by applying enhanced unified theory, and they introduced a practical factor which complements of the calculation of added resistance at short wavelengths. [Liu et al. \(2011\)](#) applied a hybrid time-domain Rankine source-Green function method to solve this basic seakeeping problem; then Maruo's approach is adopted for the calculation of added resistance. Another numerical approach is the near-field method, which calculates added resistance by integrating the second-order pressure on a body surface. [Faltinsen et al. \(1980\)](#) used the near-field approach, with good validation results. They also introduced a simplified asymptotic method to complement the deficiency of this approach in short waves. [Ye and Hsiung \(1997\)](#) applied wave Green function to the added resistance problem. These efforts on added resistance problem were mostly based on frequency-domain approaches, and have had some major successes. There were a few researches based on the Rankine panel method which is widely applied today to both linear and nonlinear ship motion problems. [Bunnik \(1999\)](#) applied Rankine panel method to calculate added resistance on ship and compared effect of linearization schemes (uniform flow, double-body flow and non-linear) on added resistance. According to this study, three different linearization schemes give similar motion responses while there are discrepancies among added resistance results; generally non-linear scheme gives good result. [Zhang et al. \(2009\)](#) used time-domain Rankine panel method to calculate the drifting forces in the horizontal plane for ships moving with forward speed. They applied both linear scheme and approximate body nonlinear scheme (hydrostatic/Froude–Krylov forces are solved over the instantaneous wetted hull surface) to calculate added resistance. [Joncquez \(2009\)](#) analyzed the added resistance problem by using a time-domain Rankine panel method, applying both far- and near-field methods. [Kim and Kim \(2011\)](#) and [Kim et al. \(2012\)](#) also applied the higher-order Rankine panel method to the added resistance problem using the far- and near-field methods. The analysis of added resistance in irregular waves was carried out, and the proper criteria of time window and number of wave frequencies were suggested for irregular waves.

Added resistance in short wavelength is another main concern on this area because it is difficult to calculate added resistance accurately using previous calculation methods. In short wavelength conditions, incident waves are almost fully reflected, and diffraction waves are mainly generated near the ship bow. This increases nonlinear effects which are not considered in the prescribed methods, resulting in a relatively large difference between the numerical results and experimental data in short wavelength. To complement this problem, a few researches were carried out. [Fujii and Takahashi \(1975\)](#) derived the semi-empirical formula of added resistance in short wavelength conditions, by adopting some complement coefficients to drift force formula of a fixed vertical cylinder. [Faltinsen et al. \(1980\)](#) also derived asymptotic formula of added resistance in short wavelength conditions by assuming that the ship has vertical side at the water plane and that the wave length is small compared to the draft of the ship. These two approaches give good results for relatively blunt bodies; however, some poor results can be obtained for fine hull like containerhips. In order to improve this drawback, the National Maritime Research Institute (NMRI) in Japan has proposed an improved expression based on the method of [Fujii and Takahashi's \(Kuroda et al., 2008, Tsujimoto et al., 2008\)](#). They modified complement coefficients using experimental data.

Recently, thanks to the rapid development of computer power, computational fluid dynamics (CFD) has been applied to some seakeeping problems. A few groups have been studying numerical

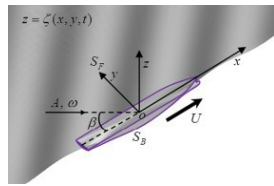
methods to solve field equations for the added resistance problem. Orihara and Miyata (2003) solved ship motions in regular head wave conditions, and evaluated the added resistance of a SR-108 containership in waves, using a CFD simulation method called WISDAM-X. The Reynolds-averaged Navier–Stokes (RANS) equation was solved by the finite-volume method with an overlapping grid system. In a recent comparative study on seakeeping computation tools (Bunnik et al., 2010), two groups – Kyushu University/Osaka University and Ecole Centrale de Nantes – calculated the added resistance of a containership in head seas. Hu and Kashiwagi (2007) developed a CFD-code which adopted a constrained interpolation profile (CIP) based Cartesian grid method. In the CIP-based formulation, the wave-body interaction problem is considered as a multi-phase problem. Different phases are recognized by a density function that has a definition similar to the volume fraction function in the VOF method. To calculate the volume fraction of solid phase, virtual particles were used. Visonneau et al. (2010) solved the trim and sink of a frigate advancing in regular head waves, using the free-surface capturing viscous solver ISIS-CFD. They used an unstructured hexahedral grid and an analytical weighting mesh deformation approach to treat the moving body problem. This program was also validated by Guo et al. (2012) for calculating the added resistance of KVLCC2 type hulls in head waves. Recently, Sadat-Hosseini et al. (2013) presented the added resistance calculation of KVLCC2 by both experiment and numerical method using CFDShip-Iowa v4.5 (Carrica et al., 2010), which is an overset, block structured CFD solver with RANS and DES for turbulence modeling and a single-phase level-set method for free-surface capturing.

In the present study, added resistances on ships have been estimated by using two numerical methods: the Rankine panel method and the Cartesian grid method (Seo et al., 2013, Yang et al., 2013). The Rankine panel method, which is based on the potential theory, is applied to solve this seakeeping problem, and to calculate the first-order potential and linear ship responses, as a necessity for the added resistance calculation. Additionally, the near-field method is adopted for the calculation of added resistance on a ship. Cartesian grid method, which solves the Euler equation directly, is also applied to estimate added resistance. In this method, the wave-body interaction problem is considered as a multiphase problem, and volume fraction functions are defined, in order to distinguish each phase in a Cartesian grid system. The added resistance is calculated by subtracting the steady surge force from the mean surge force measured in motion problems. In this study, we focus on added resistance in the short wave region, which is practically important because wave energy is concentrated. To this purpose, calculation capacities of Rankine panel method and Cartesian grid method in short wavelength are systematically analyzed using several models, including Series 60 hulls ($C_B=0.7, 0.8$), S175 containership and KVLCC2 hulls. In addition, established asymptotic methods in short wavelength are examined.

2. Mathematical background

2.1. Coordinate system

Let us consider a ship advancing with a certain forward speed, U , in the presence of incident waves. The ship's motion is defined in a mean-body fixed coordinate system, as shown in Fig. 1. Here, A , ω and β represent the incident wave amplitude, frequency and heading angle, respectively. S_B and S_F denote the body surface and the free-surface, respectively.



Download : Download full-size image

Fig. 1. Coordinate system for the ship motion problem.

The ship is assumed to have a rigid-body, and the wave-induced body motion can be written as follows:

$$\delta \rightarrow (x \rightarrow, t) = \xi \rightarrow T(t) + \xi \rightarrow R(t) \times x \rightarrow \quad (1)$$

where, $\xi \rightarrow T = (\xi_1, \xi_2, \xi_3)$ and $\xi \rightarrow R = (\xi_4, \xi_5, \xi_6)$ are rigid-body translation and rotation, respectively.

2.2. Rankine panel method

2.2.1. Boundary value problem and equation of motion

The adoption of potential theory is a typical approach for ship motion analysis. Under the assumption of incompressible, inviscid fluid with irrotational motion, the velocity potential, ϕ , can be introduced, which satisfies the following boundary value problem:

$$\nabla^2 \phi = 0 \text{ in fluid domain} \quad (2)$$

$$\phi \delta n = U \rightarrow \cdot n \rightarrow + \phi \delta \rightarrow \delta t \cdot n \rightarrow \text{ on } S_B \quad (3)$$

$$[\delta \delta t - (U \rightarrow - \nabla \phi) \cdot \nabla] [z - \zeta(x, y, t)] = 0 \text{ on } z = \zeta(x, y, t) \quad (4)$$

$$[\delta \delta t - (U \rightarrow - \nabla \phi) \cdot \nabla] \phi = -g \zeta + 1/2 \nabla \phi \cdot \nabla \phi \text{ on } z = \zeta(x, y, t) \quad (5)$$

where, S_B means the instantaneous wetted body surface, ζ and g refer to wave elevation and gravity constants, respectively. The boundary value problem can be linearized by decomposing the total velocity potential and wave elevation as follows:

$$\phi(x \rightarrow, t) = \Phi(x \rightarrow) + \phi_I(x \rightarrow, t) + \phi_d(x \rightarrow, t) \quad (6)$$

$$\zeta(x \rightarrow, t) = \zeta_I(x \rightarrow, t) + \zeta_d(x \rightarrow, t) \quad (7)$$

where, Φ indicates the basis potential, and its order is $O(1)$. ϕ_I and ζ_I denote the incident wave potential and elevation, respectively. Similarly, ϕ_d and ζ_d represent the disturbed wave potential and elevation. Both incident and disturbed components are $O(\epsilon)$. The basis potential takes uniform-flow, $-Ux$, in the Neumann–Kelvin linearization, while it takes the double-body flow potential in the double-body linearization. The linearized boundary conditions take the following forms:

$$\delta \zeta d \delta t - (U \rightarrow - \nabla \Phi) \cdot \nabla \zeta d = \delta^2 \Phi \delta z^2 \zeta d + \delta \phi d \delta z + (U \rightarrow - \nabla \Phi) \cdot \nabla \zeta I \text{ on } z = 0 \quad (8)$$

$$\delta \phi d \delta t - (U \rightarrow - \nabla \Phi) \cdot \nabla \phi d = -\delta \Phi d - \delta \zeta d + [U \rightarrow \cdot \nabla \Phi - 1/2 \nabla \Phi \cdot \nabla \Phi] + (U \rightarrow - \nabla \Phi) \cdot \nabla \phi I \text{ on } z = 0 \quad (9)$$

$$\delta \phi d \delta n = \sum_j 1/6 (\delta \xi_j \delta t n_j + \xi_j m_j) - \delta \phi I \delta n \text{ on } S^- B(m1, m2, m3) = (n \rightarrow \cdot \nabla) (U \rightarrow - \nabla \Phi)(m4, m5, m6) = (n \rightarrow \cdot \nabla) (x \rightarrow \times (U \rightarrow - \nabla \Phi)) \quad (10)$$

where, $S^- B$ is mean body surface, m_j represents the m -term, which includes effects of interaction between the steady and unsteady solutions (Nakos, 1990).

The ship motion can be obtained by solving an equation of motion as follows:

$$[M] \ddot{\xi} = [F.F.K.] + \{F.R.es.\} + \{F.H.D.\} \quad (11)$$

where, $[M]$ is the mass matrix of the ship, $\{F.F.K. \}$ and $\{F.R.es. \}$ are the Froude–Krylov force and restoring force, respectively. In the linear equation of motion, a constant restoring coefficient and a linear Froude–Krylov force are applied under the assumption that the ship motion and wave amplitude are small. $\{F.H.D. \}$ represents hydrodynamic force, except Froude–Krylov and restoring force, due to the radiation and diffraction wave of a ship.

2.2.2. Numerical implementation

To solve the prescribed linear boundary value problem, Green's second identity is applied by discretizing the boundary surface. The Rankine source ($G=1/r$) which satisfies the Laplace equation except when $r=0$ is distributed to the discretized surface, and the integral equation may then be expressed as follows:

$$\phi d + \iint S_B \phi d \delta G d n d S - \iint S_F \phi d \delta d n G d S = \iint S_B \delta \phi d \delta n G d S - \iint S_F \phi d \delta G d n d S \quad (12)$$

In the present study, physical variables, i.e. velocity potential, wave elevation and normal flux, along the fluid boundary, are approximated using the B-spline basis function.

$$\phi d(x \rightarrow, t) = \sum_j 1/9 (\phi d_j(t) B_j(x \rightarrow)) \zeta d(x \rightarrow, t) = \sum_j 1/9 (\zeta d_j(t) B_j(x \rightarrow)) \delta \phi d \delta n(x \rightarrow, t) = \sum_j 1/9 (\delta \phi d \delta n_j(t) B_j(x \rightarrow)) \quad (13)$$

where, $B_j(x \rightarrow)$ is a B-spline basis function, $(\phi d_j(t))$, $(\zeta d_j(t))$ and $(\delta \phi d \delta n_j(t))$ denote the coefficients of velocity potential, wave elevation and the normal flux at the j -th discretized boundary panel, respectively. By substituting Eq. (13) into (12) and boundary value problems described above, a matrix equation with unknown coefficients can be assembled. By solving the matrix equation, the normal flux of

velocity potential on the free-surface and the velocity potential on the body surface can be obtained. The wave elevation and velocity potential on the free-surface are then obtained by the time integration of linearized free-surface boundary conditions, Eqs. (8), (9). For the time integration of free-surface boundary conditions, a mixed explicit–implicit scheme is used. The kinematic free-surface boundary condition is solved explicitly to obtain the disturbed wave elevation on the free-surface, while the dynamic free-surface boundary condition is solved implicitly to predict the velocity potential on the free-surface in the next time step as follows:

$$\zeta_{dn+1} - \zeta_{dn} \Delta t = P(\zeta_{dn}, \phi_{dn}) \phi_{dn+1} - \phi_{dn} \Delta t = Q(\zeta_{dn+1}, \phi_{dn+1}) \quad (14)$$

where, P and Q are the forcing functions which contain all other terms in the free-surface boundary condition. In addition, the equation of motion can be solved by applying a multi-step time integration method. The 4th-order prediction–correction method is used. The radiation condition is satisfied by adopting the concept of an artificial wave absorbing zone. An artificial wave absorbing zone is distributed around the truncated boundary of the free-surface, and kinematic free-surface boundary condition is modified to include an artificial damping mechanism as follows:

$$(\delta \dot{\phi} - U \rightarrow \cdot \nabla) \zeta_d = \delta \phi_d \delta z - 2v \zeta_d + v 2g \phi_d \quad (15)$$

where, v denotes the damping strength. It is expressed as a quadratic term by using a distance between the starting point of the damping zone and the free-surface edge, therefore, the damping strength is gradually increased to the outgoing direction.

In the time-domain approach, there are no restoring forces for surge, sway, or yaw modes, and thus, a soft-spring is widely applied to restrict the divergence of the numerical solution. In the present study, the soft-spring system is applied. Linear dampings for surge, sway, roll and yaw motions are applied. The strengths of soft-spring and damping are defined as follows:

$$C_{ii} = (M_{ii} + M_{\infty, ii}) \times (2\pi T_i)^2 \text{ for } i = 1, 2, 6 \quad (16)$$

$$B_{ii} = 2\gamma (M_{ii} + M_{\infty, ii}) C_{ii} \text{ for } i = 1, 2, 4, 6 \quad (17)$$

where, M_{∞} is the infinite-frequency added mass and T_i is the soft-spring period. γ is the damping ratio which should be properly given. Details of numerical implementations are found in Kim et al. (2010) and Song et al. (2011).

2.2.3. Prediction of added resistance

In the present study, the near field method, which calculates added resistance by integrating the second-order pressure on the body surface, is applied. By using Bernoulli's equation and Taylor's series expansion, the second-order pressure can be provided for the mean body surface, and the second-order force can be obtained by integrating the second-order pressure. Added resistance can be obtained by averaging the longitudinal component of the second-order force signal. The second-order force can be formulated as follows:

$$F \rightarrow 2 = \int_{WL} \rho g (\zeta - (\xi_3 + \xi_4 y - \xi_5 x))^2 \cdot n \rightarrow dL - \rho \int_{WL} (U \rightarrow - 12 \nabla \Phi) \cdot \nabla \Phi (\zeta - (\xi_3 + \xi_4 y - \xi_5 x)) \cdot n \rightarrow dL - \rho \int_{WL} \delta \rightarrow \cdot \nabla (- (U \rightarrow - 12 \nabla \Phi) \cdot \nabla \Phi (\zeta - (\xi_3 + \xi_4 y - \xi_5 x)) \cdot n \rightarrow dL - \rho \iint S^B 12 (\nabla (\phi I + \phi_d) \cdot \nabla (\phi I + \phi_d)) \cdot n \rightarrow ds - \rho \iint S^B g z \cdot n \rightarrow 2 ds - \rho \iint S^B \delta \rightarrow \cdot \nabla (\delta (\phi I + \phi_d) \delta t - (U \rightarrow - \nabla \Phi) \cdot \nabla (\phi I + \phi_d)) \cdot n \rightarrow ds - \rho \iint S^B (g (\xi_3 + \xi_4 y - \xi_5 x) + \delta (\phi I + \phi_d) \delta t - (U \rightarrow - \nabla \Phi) \cdot \nabla (\phi I + \phi_d)) \cdot n \rightarrow 1 ds - \rho \iint S^B [(- (U \rightarrow - 12 \nabla \Phi) \cdot \nabla \Phi) \cdot n \rightarrow 2] ds - \rho \iint S^B \delta \rightarrow \cdot \nabla (- (U \rightarrow - 12 \nabla \Phi) \cdot \nabla \Phi) \cdot n \rightarrow 1 ds \quad (18)$$

where, WL and S^B represent waterline and wetted surface of the mean body, respectively. $n \rightarrow 1$ and $n \rightarrow 2$ are the first- and second-order normal vectors and expressed as follows:

$$n \rightarrow 1 = [0 - \xi_6 \xi_5 \xi_6 0 - \xi_4 - \xi_5 \xi_4 0] [n_1 n_2 n_3], n \rightarrow 2 = 12 [- (\xi_5 2 + \xi_6 2) 0 0 2 \xi_4 \xi_5 - (\xi_4 2 + \xi_6 2) 0 2 \xi_4 \xi_6 2 \xi_5 \xi_6 - (\xi_4 2 + \xi_5 2)] [n_1 n_2 n_3] \quad (19)$$

It should be noted that only a linear solution is needed for added resistance computation since the mean value of second-order solution goes to zero; therefore, there is no need to solve a complete second-order boundary value problem. Details of this formula are presented in Joncquez (2009).

2.3. Cartesian grid method

2.3.1. Flow solver

The governing equations for incompressible and inviscid fluid flow are the continuity and Euler equations, which are written in their conservative forms as follows:

$$\int \Gamma (u \rightarrow \cdot n \rightarrow) dS = 0 \quad (20)$$

$$\delta \delta t \int \Omega u \rightarrow dV + \int \Gamma u \rightarrow (u \rightarrow \cdot n \rightarrow) dS = 1 \rho [- \int \Gamma p n \rightarrow dS + \int \Omega f \rightarrow b dV] \quad (21)$$

where, Ω indicates a control volume, and Γ means the control surface enclosing the control volume. $n \rightarrow$ is a unit outward normal vector on Γ , ρ is the fluid density, and p and $u \rightarrow$ denote the pressure and velocity vector, respectively. In addition, $f \rightarrow b$ indicates the body force vector.

Velocity and pressure are coupled by a fractional step method, involving a solving procedure which is divided into three steps, one advection and two non-advection phases, as follows:

$$\int \Omega u \rightarrow \rightarrow dV - \int \Omega u \rightarrow ndV \Delta t + \int \Gamma u \rightarrow (u \rightarrow \cdot n \rightarrow) dS = 0 \quad (22)$$

$$\int \Omega u \rightarrow \rightarrow \rightarrow dV - \int \Omega u \rightarrow \rightarrow dV \Delta t = 1 \rho n + 1 \int \Omega f \rightarrow b dV \quad (23)$$

$$\int \Omega u \rightarrow n + 1 dV - \int \Omega u \rightarrow \rightarrow \rightarrow dV \Delta t = -1 \rho n + 1 \int \Gamma p n \rightarrow 1 n \rightarrow dS \quad (24)$$

Superscripts $(\ast, \ast\ast, n, n+1)$ indicate intermediate values during time advancement. The pressure field is calculated through solving the pressure Poisson equation, which is obtained by taking the divergence of Eq. (24), and using the continuity equation and the divergence theorem.

$$\nabla (1 \rho n + 1 \int \Gamma p n \rightarrow 1 n \rightarrow dS) = 1 \Delta t \int \Gamma u \rightarrow \ast\ast \cdot n \rightarrow dS \quad (25)$$

Spatial discretization is carried out based on the finite volume approach with staggered variable allocation. The surface integration is approximated by using a midpoint rule, and the cell center value for the convective term is interpolated with a monotonic central (MC) limiter function (Waterson and Deconinck, 2007). A directional splitting approach is applied in order to consider multidimensional effects, and further spatial discretization is conducted based on the second-order central difference scheme.

The free surface is determined by an interface capturing method. To identify the different phases in the multi-phase flow, density functions, γ_m are defined for liquid ($m=1$), gas ($m=2$) and solid bodies ($m=3$). The density function for the liquid phase is calculated by solving the following advection equation:

$$\delta \gamma 1 \delta t + u \rightarrow \cdot \nabla \gamma 1 = 0 \quad (26)$$

To solve this advection equation, various numerical methods have been proposed in literature. Among them, the tangent of hyperbola for interface capturing (THINC) scheme introduced by Xiao et al. (2005) is used in the present computation. The basic idea of the THINC method is that the density function profile inside of a computational cell is approximated as a hyperbolic tangent function to reproduce the jump of density function near the free surface. Yokoi (2007) developed an improved multi-dimensional THINC scheme by adapting the weighed line interface calculation (WLIC) method, which takes into account information of the surface normal vector, while maintaining a simple implementation. The THINC method combined with the WLIC method is used throughout the computation.

Incident waves are generated from the left wall of the domain. The boundary conditions for the velocity and the density function of the liquid phase can be calculated from Stokes' linear wave solution. The domain stretched method is adopted to apply the linearized solution above the mean-water level, and the incident velocity is adjusted so that the net flux during one period is maintained as zero. In order to simulate more than 20 wave periods without reflected waves, a damping zone is located far from the ship. In the damping zone behind the ship region, a damping force is applied on the total velocity component while the damping force is acted on velocity component subtracting linear incident wave solution from the total velocity near the incident wave generating region.

2.3.2. Treatment of complex geometry

An arbitrary body is embedded in a Cartesian-grid system, and is identified by a volume fraction function of the solid body. To calculate the volume fraction of the solid body in each cell, a level-set-based method is applied. The first step of calculating the signed distance field is to read the geometric information of a solid body, represented by a triangular surface mesh. For grid points near each triangular surface, the distance field is calculated by transformation of the given triangle to a unit right triangle, and defining the quadratic distance function, which has minimum value when the gradient of the quadratic function equals zero. When the minimum value is located inside the transformed triangle, inverse transformation gives the coordinates of the closest point corresponding to a grid point. Otherwise, the intersection point of a triangle edge or vertex with contour line should be obtained. To determine whether the grid point is inside or outside the body, the sign of the inner product of the outward normal vector, and the direction vector between the grid point and the corresponding closest point is checked. When the closest point is located at a triangle edge or vertex, another definition of the normal vector is needed. The angle-weighted pseudo-normal vector introduced by Bærentzen and Aanaes (2005) is used in this study, and is defined at each triangle vertex and edge. After obtaining the signed distance field from the triangular surface for each grid point, the volume fraction function can be calculated by using a smoothed Heaviside function (Yang et al., 2013).

To impose a no-slip boundary condition on the ship surface, a volume-weighted formulation is used.

$$u \rightarrow \wedge = u \rightarrow (1 - \gamma 3 u \rightarrow) + U \rightarrow body \gamma 3 u \rightarrow \quad (27)$$

where, $u \rightarrow \wedge$ is the corrected velocity, $U \rightarrow body$ is the body velocity and $\gamma 3 u \rightarrow$ is the volume fraction of the body in the corresponding control volume of velocity components. The force and moment

acting on the body are calculated as follows:

$$F \rightarrow - \iint_{SB} p n \rightarrow dS = - \sum_l \frac{1}{n} \text{Face} p n \rightarrow l \Delta S_l \quad (28)$$

$$M \rightarrow - \iint_{SB} (x \rightarrow x \rightarrow c_g) \times (p n \rightarrow) dS = - \sum_l \frac{1}{n} \text{Face} (x \rightarrow x \rightarrow c_g) \times n \rightarrow l p l \Delta S_l \quad (29)$$

where, $n \text{Face}$ indicates the number of triangular surfaces, p_l $n \rightarrow l$, and ΔS_l means the normal vector, interpolated pressure, and area of the l -th triangular surface, respectively. $x \rightarrow l c$ is the center coordinate of each triangular surface. Added resistance is calculated by a direct pressure integration method, which means that the resistance is calculated from the surface integration of pressure. The mean surge force is calculated under the certain incident wave conditions and forward speed. Then, the mean steady force is also calculated in calm water with the same forward speed, and subtracting the mean steady force from the mean surge force in waves provides the added resistance of a given wave condition. It should be noted that the absolute value of mean steady force is not important because the viscous effects are ignored in the present method. However, the grid system and the size of time window for calm water calculations should be the same with those for incident wave condition.

Fig. 2 shows the flow chart of the Cartesian grid method. The program starts with reading input, mesh, and geometry files. The input file contains the calculation conditions, such as wave condition, ship particulars and other parameters. The mesh file simply has Cartesian grid information and the geometry file is an STL format file which contains coordinates of vertex points and outward unit normal vectors. The main calculation is composed of two basic parts – flow solver and body treatment. In the first part, the fluid flow problem is solved for a fixed body configuration, and the body position is updated in the second part, as explained in the previous section. Then, the time increases by the time step size, which is determined to satisfy the CFL condition. This calculation is repeated until the final time.

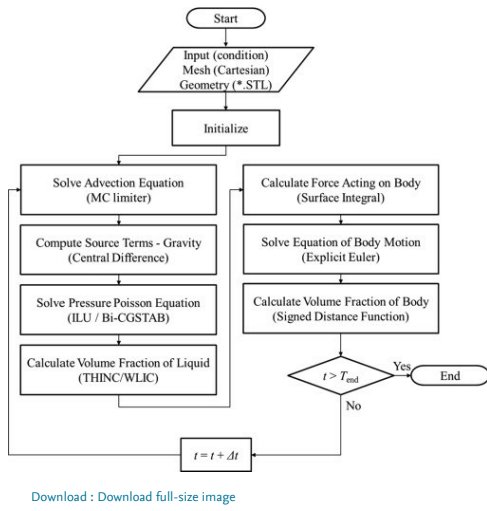


Fig. 2. Flow chart of the present Cartesian grid method.

2.4. Prediction methods for added resistance in short wavelength

In short wavelengths, it is difficult to calculate added resistance accurately because hydrodynamic nonlinear effects are intensified at bow diffraction waves. To complement this difficulty, a few researches are carried out. Faltinsen et al. (1980) derived asymptotic formula of added resistance in short wave. They assumed that the ship has vertical sides at the water plane, and the wave length is small compared to the draft of the ship. Due to the small wave length assumptions, the influence of the wave induced motions can be neglected, as only the part of the ship close to the water plane will affect the flow field. From this, the following asymptotic formula can be derived.

$$R = 12 \rho g \zeta^2 l [\sin 2(\theta - \beta) + 2\omega U g [1 + \cos \theta \cos(\theta - \beta)]] n \rightarrow d \ln 1 = \sin \theta n 2 - \cos \theta n 6 = x 0 \cos \theta - y 0 \sin \theta \quad (30)$$

where, θ is the waterline inclined angle, and β is wave incident angle, defined in Fig. 3. The integration in Eq. (30) is performed over the non-shaded part (A-F-B) of the waterline (Fig. 3).

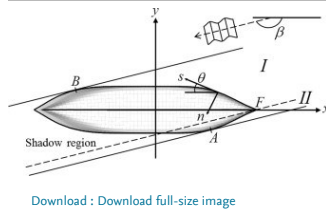


Fig. 3. Coordinate system for the added resistance calculation in the short wave region (Faltinsen et al., 1980).

Fujii and Takahashi (1975) derived the semi-empirical formula of added resistance in short wave conditions by adopting some complement coefficients to the drifting force formula of a fixed vertical cylinder. The National Maritime Research Institute (NMRI) in Japan proposed an improved expression based on the method of Fujii and Takahashi's (1975), by modifying compliment coefficients (Kuroda et al., 2008, Tsujimoto et al., 2008). These two formulas can be expressed as follows:

$$R = \alpha d (1 + \alpha U) [12 \rho g \zeta^2 B f(\beta)] \quad (31)$$

$$\text{Method of Fujii and Takahashi } B f(\beta) = 1 B [I \sin 2(\theta - \beta) \sin \theta d l + I I \sin 2(\theta + \beta) \sin \theta d l] \alpha d = n 2 I 1 2(k d) n 2 I 1 2(k d) + K 1 2(k d) 1 + \alpha U = 1 + 5 F n \quad (32)$$

$$\text{Method of NMRI } B f(\beta) = 1 B [I \sin 2(\theta - \beta) \sin \theta d l + I I \sin 2(\theta + \beta) \sin \theta d l] \alpha d = n 2 I 1 2(k d) n 2 I 1 2(k d) + K 1 2(k d), (k c = \omega c 2 g) 1 + \alpha U = 1 + C U F n, (C U = \max[10.0, -310 B f(\beta) + 68]) \quad (33)$$

These formulas comprise B_f the bluntness coefficient; α_d the reflection coefficient composed of ship draft and wave number; and $1 + \alpha_u$ the advance speed coefficient. The integration is performed over parts I and II, which means the non-shade port part and the starboard part, respectively. I , K_1 represents modified Bessel function of the first kind of order 1 and modified Bessel function of the second kind of order 1, respectively. In the method of the NMRI, the advance speed coefficient and the reflection coefficient are modified. A regression coefficient, C_U , which is decided using experimental data, is proposed in the advance speed coefficient. Also encounter wave number k_e is substituted for wave number k in the reflection coefficient, α_d . This means that the effect of advance speed is added not only to the advance speed coefficient, $1 + \alpha_u$ but also to the reflection coefficient, α_d .

3. Numerical results

3.1. Test models

In order to verify and validate the developed program, several test models are considered; Series 60 with block coefficient 0.7, 0.8, S175 containership and KVLCC2. The main particulars of test models are summarized in Table 1. One of test model, KVLCC2, has immersed transom and viscous effects are dominant in this region. In this case, Rankine panel method cannot accurately solve this transom flow. The effect of transom stern, however, is localized and does not affect the global solution (Mantzaris, 1998). Moreover, in added resistance problem, radiation wave and diffracted wave at bow is much more important than steady stern flow; therefore, exact flow pattern near the transom stern does not considered in this study. The present computation starts from the validation of the motion response, since motion response is a crucial influence upon added resistance. To this end, the computed motion responses of test ships are compared with experimental data, and added resistances on ships are then observed in regular waves.

Table 1. Main dimension of test models.

Model	Series60 $C_F=0.7$	Series60 $C_F=0.8$	S175 containership	KVLCC2
$L(m)$	100.0	100.0	175.0	320.0
$B(m)$	14.29	15.39	25.4	58.0
$D(m)$	5.72	6.15	9.5	20.8
C_B	0.7	0.8	0.561	0.8098

An example of solution grids are shown in Fig. 4. Fig. 4(a) shows the panel model used in the Rankine panel method. The number of panels varies, depending on body shape and wave length, and about 6000 panels are applied for a half domain. Fig. 4(b) shows the typical grid system used in the Cartesian grid method. Even though the number of grids depends on wave length and wave amplitude, the average number of grid is about 4 million to 5 million ($280 \times 130 \times 130$). Most of them are clustered near the ship and free-surface region.

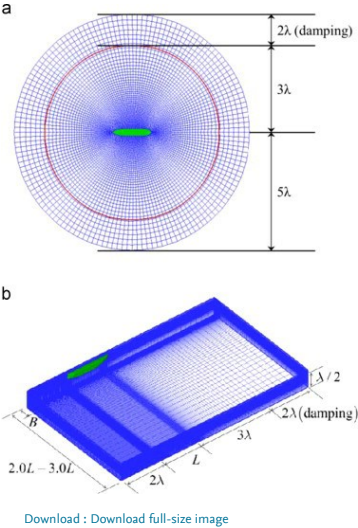
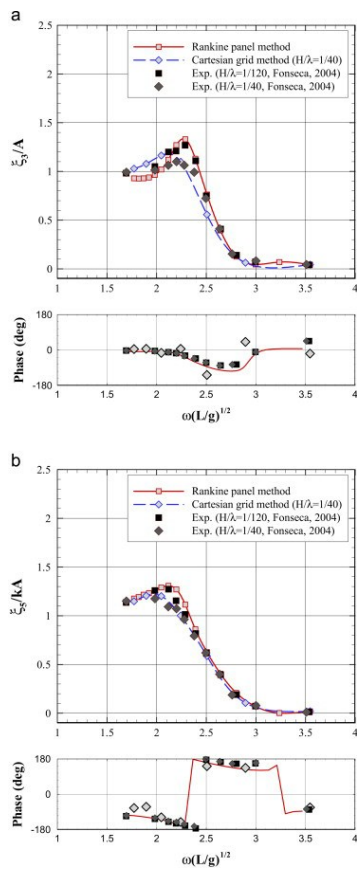


Fig. 4. Examples of solution grid (KVLCC2 model). (a) Panel model for Rankine panel method. (b) Grid distribution for Cartesian grid method.

3.2. Motion response in regular waves

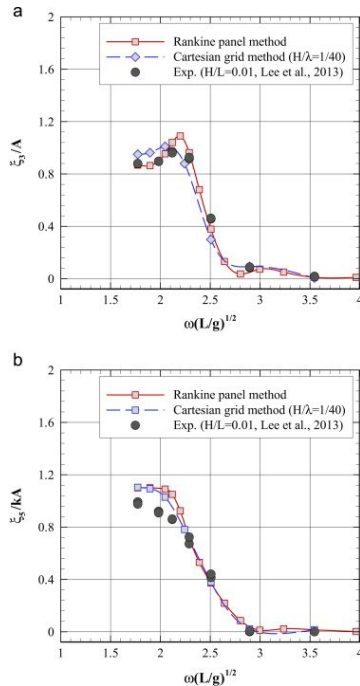
The ship motion response is directly related to added resistance, especially, the radiation component of added resistance. The exact calculation of the ship motion response, therefore, is important to accurately predict the added resistance. The validation of the ship motion response is carried out in this section. In the present study, the Rankine panel method and Cartesian grid method are applied to analyze the ship motion problem. To validate the ship motion responses, heave and pitch motions calculated by each methods are compared with experimental data.

Fig. 5, Fig. 6 show the vertical motion responses of a S175 containership at $Fn=0.25$ and KVLCC2 at $Fn=0.142$, respectively. As shown in these figures, overall tendencies of the motion responses are similar to each other, and show good agreement with experimental data. In the case of S175 containerships, there are two experimental data which are conducted by Fonseca and Soares (2004); one is that the ratio of wave height to wave length is 1:40 ($H/\lambda=1/40$) which is the same condition with Cartesian grid method, and the other is that the ratio of wave height to wave length is 1:120 ($H/\lambda=1/120$) which can be said to be a linear condition. It can be easily predicted that experimental data of higher wave conditions ($H/\lambda=1/40$) would result in a similar outcome to that of the Cartesian grid method, while experimental data of lower wave conditions ($H/\lambda=1/120$) would result in an outcome similar to that of the Rankine panel method. In the case of phase angle, both computation results are well agreed with experimental data. According to Fonseca and Soares (2004), wave steepness affects mainly on motion response around the resonance frequency, and there is no significant effect on phase angles.



[Download : Download full-size image](#)

Fig. 5. Vertical motions of S175 containership ($F_n=0.25$, $\beta=180^\circ$). (a) Heave motion RAOs and phase angles. (b) Pitch motion RAOs and phase angles.



[Download : Download full-size image](#)

Fig. 6. Vertical motions of KVLCC2 ($F_n=0.142$, $\beta=180^\circ$). (a) Heave motion RAOs. (b) Pitch motion RAOs.

3.3. Grid convergence test

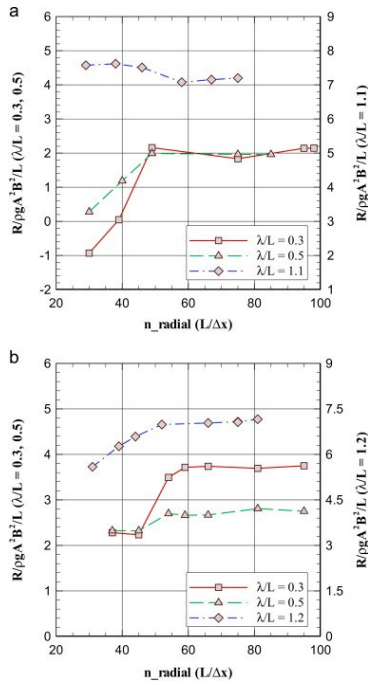
As mentioned above, it is more difficult to calculate added resistance accurately than motion response because added resistance is a second-order value. Therefore, it is needed to check grid convergence of added resistance. In this section, results of grid convergence test are presented using several model ships.

3.3.1. Rankine panel method

In the case of the Rankine panel method, panels should be distributed at the free-surface and body surface. Distributed panel size and shape crucially affect the calculation results, especially in added resistance. In the present computation, panels are concentrated at bow and stern because changes of body shape at bow and stern are much more severe than those at the mid-ship region. Furthermore, the domain size of the free-surface is 5–6 times larger than the incident wave length including the numerical damping zone.

First of all, it is needed to check how many panels should be distributed at each calculation condition. To confirm this, grid convergence tests are conducted using several model ships. Fig. 7 shows the results of convergence testing. Series60 ($C_F=0.8$) and KVLCC2 hulls were applied to the convergence test, and 3 different wavelengths were chosen: $\lambda/L=0.3$, 0.5 and peak value wavelength of added resistance on each ship. In these figures, x -axis means number of panels with respect to radial direction. When n_{radial} increases, both numbers of body and free-surface panels increase too. The

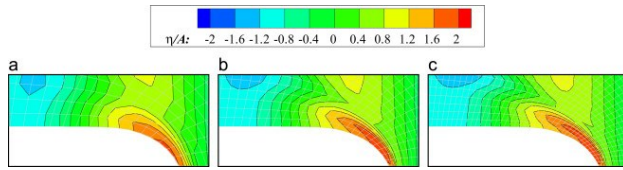
number of body panels increases about 200–1000, the number of free-surface panels increases about 1000–6000; therefore, total panel number is about 1000–7000. In the present Rankine panel method, the O-type panel is used; therefore, number of panels with respect to radial direction is equal to the number of x-directional panels near the body (refer to Fig. 4(a)). As shown in these figures, it is desirable that more than 60 panels should be distributed to radial direction. Another thing to note is that much more panel should be needed to converge in short wavelength conditions.



Download : [Download full-size image](#)

Fig. 7. Grid convergence tests for added resistance computation. (a) Series60 with $C_B=0.8$, $Fn=0.15$. (b) KVLCC2, $Fn=0.142$.

Fig. 8 shows the comparison of wave contour near the bow region for three different panel systems. The target ship is one with a KVLCC2 hull, and the wave condition is $\lambda/L=0.5$. Most wave patterns are similar to each other, while the difference can be found near the bow region. In the finest case, generated waves are slightly higher at the bow region and more dispersed backwards than in other cases. It seems that these differences in wave patterns near the bow region result in different figures for added resistance.



Download : [Download full-size image](#)

Fig. 8. Comparison of wave contours near the ship bow region for different panel distributions (KVLCC2, $Fn=0.142$, $\lambda/L=0.5$). (a) $L/\Delta x=37$, (b) $L/\Delta x=59$, (c) $L/\Delta x=95$.

Next, wave elevation and pressure on the body surface are checked because these values are important for the calculation of added resistance. Fig. 9 shows wave elevation and pressure on the body, which is calculated under two wave conditions, where the ratio of wavelength to ship length is 0.4 and 1.0. As shown in these figures, spatial variations of wave elevation and pressure at short wavelength are more severe than those at long wavelength, and therefore, we can draw same conclusions as previous convergence testing, that much more panel should be distributed when the incident wave length is short.

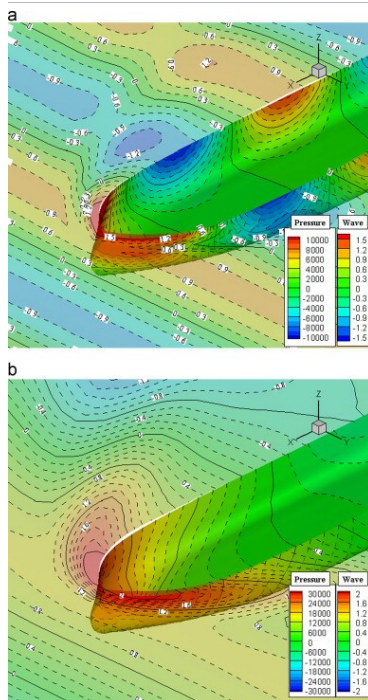


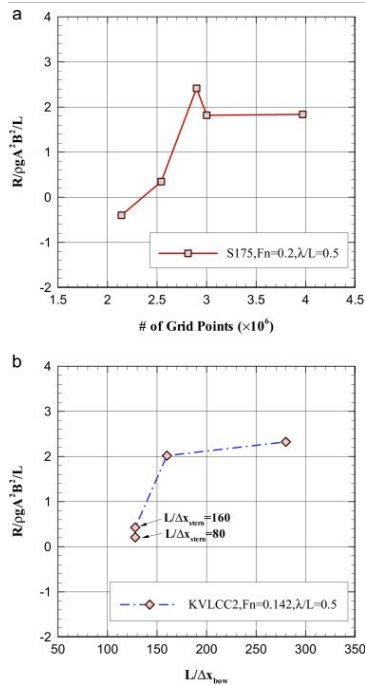
Fig. 9. Wave elevation and pressure distribution on KVLCC2 ($F_n=0.142$, $\beta=180^\circ$). (a) $\lambda/L=0.4$. (b) $\lambda/L=1.0$.

3.3.2. Cartesian grid method

The absolute magnitude of added resistance is quite small compared to other force components. Thus, it is necessary to carry out grid dependency testing for calculating the added resistance, and in order to obtain a reliable value. Grid conditions for grid convergence testing of S175 containership are given in Table 2. The number of mesh points is varied from two million to four million. The added resistance values for each grid system are plotted in Fig. 10 and the converged solution can be obtained after three million grid points. The longitudinal (x -) and vertical (z -) direction grid sizes have significant influence upon the added resistance value compared to the span wise (y -) direction grid spacing. Based on this test, the same grid system is used for KVLCC2 calculation. However, KVLCC2 has blunt bow shapes while S175 containership has slender bow shapes. Thus, the added resistance of KVLCC2 is quite sensitive to the grid spacing near the bow region, as shown in Fig. 10. Four different grid systems are used for KVLCC2 calculations. “ $dx0$ ” case has the same grid resolution with that of S175 case, which provides a converged solution. The only difference between “ $dx0$ ” case ($L/\Delta x_{bow}=128$) and the other cases – “ $dx1$ ” ($L/\Delta x_{bow}=160$) and “ $dx2$ ” ($L/\Delta x_{bow}=280$) – is the longitudinal (x -) direction grid resolution near the ship bow region. For “ $dx0$ ” case, two different grid spacings exist near the stern region, but the difference between them is not severe.

Table 2. Conditions for grid dependency test (S175 containership, $F_n=0.2$, $\lambda/L=0.5$).

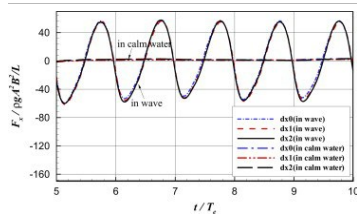
Index	$L/\Delta x$	$L/\Delta y$	$L/\Delta z$	Total mesh
Grid1	78.9	29.0	6.7	2,140,800
Grid2_x	145.8	29.0	6.7	2,899,200
Grid2_y	78.9	40.0	6.7	2,542,200
Grid2_z	116.7	29.0	10.9	3,000,512
Grid3	145.8	40.0	10.9	3,970,696



Download : Download full-size image

Fig. 10. Grid convergence test of added resistance ($H/\lambda=1/40$, $\lambda/L=0.5$). (a) S175 containership, $F_n=0.2$. (b) KVLCC2, $F_n=0.142$.

The comparison of surge force signal for different longitudinal grids near the bow region is presented in Fig. 11. Three different grid systems provide very similar force signals, and the difference is order of one in terms of normalized value. However, this difference resulted in totally different added resistance values, as shown in Fig. 10. It should be noted that negative wave making resistance (due to the coordinate system it is positive value in Fig. 11) in calm water condition is obtained in this calculation because the viscosity is ignored in the present method. Generally, wave making resistance is quite small compared to viscous drag for a blunt ship with slow forward speed like KVLCC2. Also, it is very sensitive to grid resolution not only near the ship bow region but also around stern region. However, added resistance in short wave is sensitive primarily to grid resolution near the ship bow region. In our computation, we could provide enough grids near the ship bow region only because of computing capacity. Although convergent resistance in calm water is not obtained within our computational capacity, added resistance is obtained by using similar grid system near the body for calm water condition and incident wave condition.

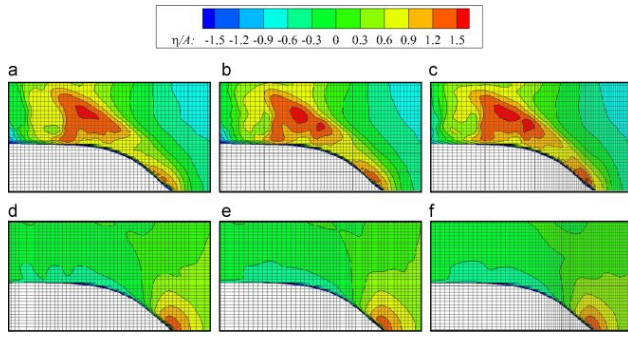


Download : Download full-size image

Fig. 11. Comparison of surge forces for different grid systems (KVLCC2, $F_n=0.142$, $\lambda/L=0.5$, $H/\lambda=1/40$).

Fig. 12 shows the comparison of wave contour near the bow region for three different grid systems. Most wave patterns are very similar to each other both in calm water and in wave conditions, but the difference can be found near the ship surface of the bow region in the presence of incident wave. Wave elevations differ slightly to each other, and the finest case shows slightly higher wave elevation

than the other cases. It increases the added resistance since the waterline integration of the wave elevation is a dominant component of the added resistance.



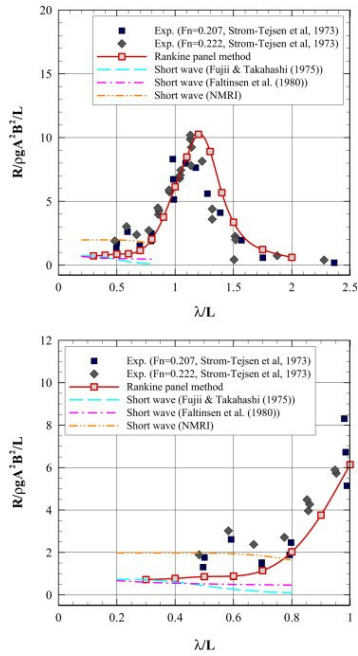
[Download : Download full-size image](#)

Fig. 12. Comparison of wave contour near the ship bow region for different grid systems (KVLCC2, $Fn=0.142$, $\lambda/L=0.5$, $H/\lambda=1/40$). (a) $dx0$: $L/\Delta x_{bow}=128$ (in wave), (b) $dx1$: $L/\Delta x_{bow}=160$ (in wave), (c) $dx2$: $L/\Delta x_{bow}=280$ (in wave), (d) $L/\Delta x_{bow}=128$ (in calm water), (e) $L/\Delta x_{bow}=160$ (in calm water), (f) $L/\Delta x_{bow}=280$ (in calm water).

3.4. Added resistance in regular waves

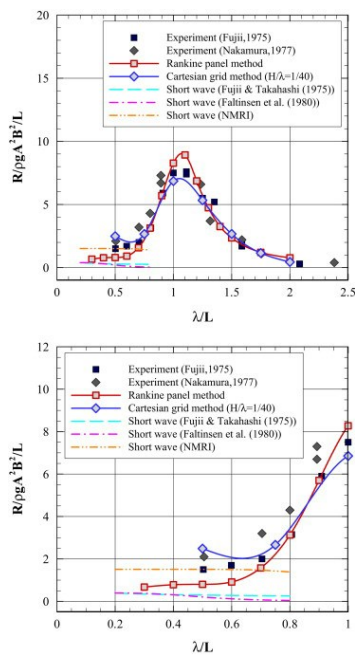
To compare the capability and accuracy of the prediction of added resistance between the numerical methods, the computational results of added resistances on Series 60 ($C_F=0.7, 0.8$), S175 containership and KVLCC2 are compared with the experimental data. Only the S175, KVLCC2 cases are considered in the Cartesian grid method. Typical computation times of Rankine panel method are less than 1 min per wave periods with 5000–6000 panels, and typical computation times of Cartesian grid method are about 12 h per one wave period with 4–5 million grid points.

Fig. 13, Fig. 14 show the results of added resistance on Series 60 ($C_F=0.7$) with $Fn=0.222$, and S175 containership with $Fn=0.2$. These two ships have relatively slender bodies. In these figures, x - and y -axes represent the non-dimensional wavelength and added resistance, respectively. The red solid line with square symbol is the result of the Rankine panel method and the blue solid line with diamond symbol is result of Cartesian grid method. As shown in these figures, results of both numerical methods show reasonable agreements with experimental data.



[Download : Download full-size image](#)

Fig. 13. Added resistance on Series 60 with $C_F=0.7$ ($Fn=0.222$, $\beta=180^\circ$). (For interpretation of the references to color in this figure, the reader is referred to the web version of this article.)

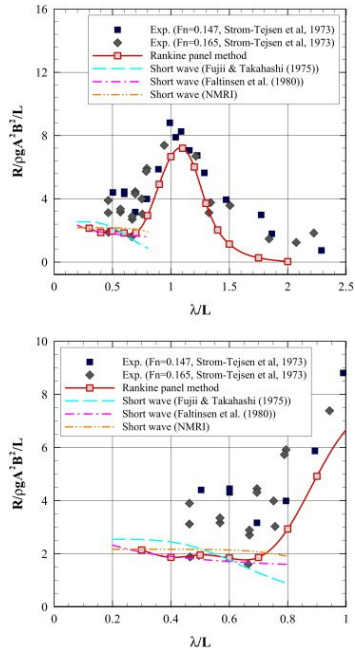


[Download : Download full-size image](#)

Fig. 14. Added resistance on S175 containership ($F_n=0.2$, $\beta=180^\circ$). (For interpretation of the references to color in this figure, the reader is referred to the web version of this article.)

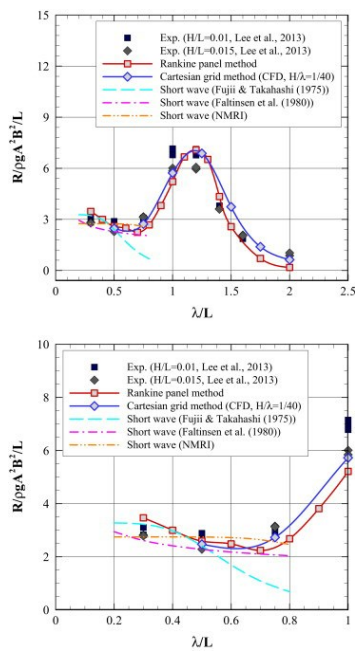
The short wave region, where the wavelength is less than ship length, is practically important because wave energy is concentrated in this region. Added resistances in short wavelength are presented in right hand side figures, which are enlarged from left hand side figures. In these figures, five calculation methods are applied: the Rankine panel method and Cartesian grid method are valid for whole wavelength, and three asymptotic formulas are only valid for short wave region. In the case of short wave calculation, only the results of NMRI's method are in good agreement with experimental data. It has already been mentioned that the method of Fujii and Takahashi (1975) and that of Faltinsen et al. (1980) give good agreements with measured data for relatively blunt bodies, while some poor agreements are obtained for slender hulls. NMRI's method, however, gives good agreement for a slender body too, because they supplemented their formula using experimental data. Added resistance in short wavelength calculated by Rankine panel method shows smaller values than experimental data, whereas the magnitude of it is similar to the results of Fujii and Takahashi (1975) as well as those of Faltinsen et al. (1980). While the Cartesian grid method applied to short wavelength conditions provides similar results to experimental data and NMRI's result.

Fig. 15, Fig. 16 show the results of added resistance on Series60 ($C_F=0.8$) with $F_n=0.15$ and KVLCC2 with $F_n=0.142$. These two vessels have relatively blunt bodies. In the case of Series60 ($C_F=0.8$), the magnitude of added resistance calculated Rankine panel method is smaller than the experimental data, while overall tendency is similar to experimental data. Also, in short wavelength, the results of Rankine panel method gives similar values with short wave calculation methods. In the case of KVLCC2, both the Rankine panel method and Cartesian grid method give good agreement with experimental data. In addition, added resistances in short wavelength calculated by the Rankine panel method and Cartesian grid method show similar results of short wave calculation methods and are in good agreement with experimental data.



[Download : Download full-size image](#)

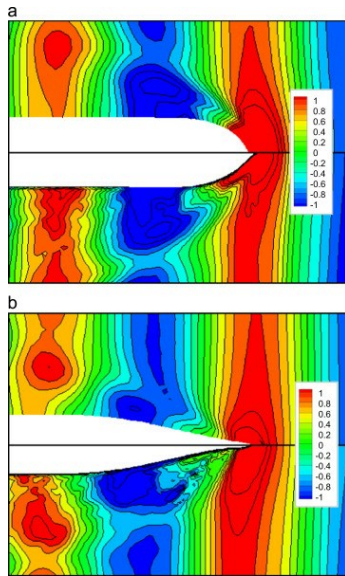
Fig. 15. Added resistance on Series 60 with $C_F=0.8$ ($F_n=0.15$, $\beta=180^\circ$).



Download : [Download full-size image](#)

Fig. 16. Added resistance on KVLCC2 ($F_n=0.142$, $\beta=180^\circ$).

As shown in Fig. 13, Fig. 14, Fig. 15, Fig. 16, if the vessel has a blunt body, all computational results calculated in short wavelength conditions show reasonable agreement with experimental data, while the Cartesian grid method and NMRI method give good results in short wavelength conditions when the vessel has a slender body. This means that a non-linear effect, which is not included in the potential based solver is important in the added resistance on slender bodies in short wavelength conditions. To confirm this, wave contours computed by the Rankine panel method (upper) and Cartesian grid method (lower) are compared in Fig. 17. Fig. 17(a) shows wave contours near the S175 containership and (b) shows wave contours near the KVLCC2. Wave conditions of both cases are $\lambda/L=0.5$. As shown in these figures, wave contours near the KVLCC2 are similar to each other, while wave contours near the S175 are a little bit different. The Cartesian grid method gives more complicated wave elevation near the bow, and this result in a different added resistance.



Download : [Download full-size image](#)

Fig. 17. Comparison of wave contour calculated by Rankine panel method (upper) and Cartesian grid method (lower). (a) S175 containership, $F_n=0.2$, $\lambda/L=0.5$. (b) KVLCC2, $F_n=0.142$, $\lambda/L=0.5$.

4. Conclusion

The potential-based Rankine panel method and FV-based Cartesian-grid method were applied to calculate ship motion and added resistance. Using both methods, motion responses were validated for several ship models, and the added resistance was estimated, especially focusing on short wave cases. Asymptotic formulas, which are only valid in the short wave region, were also adopted for comparison. Based on the present study, the following conclusions can be obtained:






- Numerical results of ship motion response and added resistance, which were obtained using the Rankine panel method and Cartesian grid method, showed reasonable agreement with experimental data. To predict the reliable added resistance, grid convergence testing should be conducted, because the added resistance is sensitive to the panel size or grid spacing. Especially, a ship which has a blunt bow shape requires a finer grid near the ship bow region.
- According to grid convergence test of the Rankine panel method, more panels are required in short wave conditions than in long wave conditions. This is because spatial variations of physical variables, such as wave elevation, are more severe on the body surface in the short wave region, than in the long wave region. Also, it is recommended that panels are concentrated on bow and stern because change of body shape at bow and stern is much more severe than those in the mid-ship region.
- According to results of added resistance in the short wave region, all computational methods gave good results when the vessel has a blunt body, while only the Cartesian grid method and short wave calculation method proposed by the NMRI provided good results when the vessel has a slender body. The Cartesian grid method can predict an added resistance which is similar to the experimental data, regardless of the vessel's bluntness, if the grid resolution is enough to capture the local flow near the ship bow region. This implies that nonlinear effects, which are not included in potential based solvers importantly influence added resistance on a slender body in short wavelength conditions.

Acknowledgment

This study has been partly supported by the Korean Ministry of Knowledge Economy (MKE), Project number [10040030](#), and also partly supported by the LRF*-Funded Research Center at Seoul National University. Their support is greatly appreciated. The administrative support of RIMSE and ERI are also acknowledged. (* Lloyd's Register Foundation(LRF): a UK registered charity and sole shareholder of Lloyd's Register Group Ltd., invests in science, engineering and technology for public benefit, worldwide).

[Recommended articles](#) [Citing articles \(41\)](#)

References

- [Bærentzen and Aanaes, 2005](#) J.A. Bærentzen, H. Aanaes
Signed distance computation using the angle weighted pseudonormal
 IEEE Trans. Vis. Comput. Graph., 11 (3) (2005), pp. 243-253
[View Record in Scopus](#) [Google Scholar](#)
- [Bunnik, 1999](#) T. Bunnik
Seakeeping Calculations For Ships, Taking Into Account the Non-linear Steady Waves (Ph.D. thesis)
 Delft University of Technology, Delft, Netherlands (1999)
[Google Scholar](#)
- [Bunnik et al., 2010](#) Bunnik, T., Daalen, E. van Kapsenberg, G., Shin, Y., Huijsmans, R., Deng, G., Delhommeau, G., Kashiwagi, M., Beck, B., 2010. A comparative study on state-of-the-art prediction tools for seakeeping. In: Proceedings of the 28th Symposium on Naval Hydrodynamics. California, USA, pp. 1–13.
[Google Scholar](#)
- [Carrica et al., 2010](#) P.M. Carrica, J. Huang, R. Noack, D. Kaushik, B. Smith, F. Stern
Large-scale DES computations of the forward speed diffraction and pitch and heave problems for a surface combatant
 Comput. Fluids, 39 (7) (2010), pp. 1095-1111
[Article](#)  [Download PDF](#) [View Record in Scopus](#) [Google Scholar](#)
- [Faltinsen et al., 1980](#) Faltinsen, O.M., Minsaas, K.J., Liapis, N., Skjoldal, S.O., 1980. Prediction of resistance and propulsion of a ship in a seaway. In: Proceedings of the 13th Symposium on Naval Hydrodynamics. Tokyo, Japan, pp. 505–529.
[Google Scholar](#)
- [Fonseca and Soares, 2004](#) N. Fonseca, C.G. Soares
Experimental investigation of the nonlinear effects on the vertical motions and loads of a containership in regular waves
 J. Ship Res., 48 (2) (2004), pp. 118-147
[CrossRef](#) [View Record in Scopus](#) [Google Scholar](#)
- [Fujii and Takahashi, 1975](#) Fujii, H., Takahashi, T., 1975. Experimental study on the resistance increase of a ship in regular oblique waves. In: Proceeding of the 14th International Towing Tank Conference (ITTC1975). Ottawa, Canada, pp. 351–360.
[Google Scholar](#)
- [Gerritsma and Beukelman, 1972](#) J. Gerritsma, W. Beukelman
Analysis of the resistance increase in waves of a fast cargo ship
 Int. Shipbuild. Prog., 19 (217) (1972), pp. 285-293
[CrossRef](#) [View Record in Scopus](#) [Google Scholar](#)
- [Guo and Steen, 2011](#) B.J. Guo, S. Steen
Evaluation of added resistance of KVLCC2 in short waves
 J. Hydrodyn., 23 (6) (2011), pp. 709-722
[Article](#)  [Download PDF](#) [CrossRef](#) [View Record in Scopus](#) [Google Scholar](#)
- [Guo et al., 2012](#) B.J. Guo, S. Steen, G.B. Deng
Seakeeping prediction of KVLCC2 in head waves with RANS
 Appl. Ocean Res., 35 (2012), pp. 56-67
[Article](#)  [Download PDF](#) [View Record in Scopus](#) [Google Scholar](#)
- [Hu and Kashiwagi, 2007](#) Hu, C., Kashiwagi, M., 2007. Numerical and experimental studies on three-dimensional water on deck with a modified wigley model. In: Proceedings of the 9th International Conference on Numerical Ship Hydrodynamics. Michigan.
[Google Scholar](#)
- [Joncquez, 2009](#) S.A.G. Joncquez
Second-Order Forces and Moments Acting on Ships in Waves (Ph.D. thesis)
 Technical University of Denmark, Copenhagen, Denmark (2009)
[Google Scholar](#)
- [Journee, 1992](#) Journee, J.M.J., 1992. Experiments and calculations on four Wigley hull forms. Delft University of Technology Report.
[Google Scholar](#)
- [Kashiwagi et al., 2009](#) Kashiwagi, M., Takehiro, I., Takuma, S., 2009. Effect of forward speed of a ship on added resistance in waves. In: Proceedings of the 19th International Offshore and Polar Engineering Conference. Osaka, Japan, pp. 818–825.
[Google Scholar](#)
- [Kim and Kim, 2011](#) K.H. Kim, Y. Kim
Numerical study on added resistance of ships by using a time-domain Rankine panel method
 Ocean Eng., 38 (2011), pp. 1357-1367
[Article](#)  [Download PDF](#) [View Record in Scopus](#) [Google Scholar](#)
- [Kim et al., 2012](#) K.H. Kim, M.G. Seo, Y. Kim
Numerical analysis on added resistance of ships
 Int. J. Offshore Polar Eng., 21 (1) (2012), pp. 21-29
[View Record in Scopus](#) [Google Scholar](#)
- [Kim et al., 2010](#) Kim, Y., Kim, K.H., Kim, J.H., Kim, T.Y., Seo, M.G., Kim, Y., 2010. Time-domain analysis of nonlinear motion responses and structural loads on ships and offshore structures: development of WISH programs. In: Proceedings of the ITTC Workshop on Seakeeping. Seoul, Korea, pp. 19–21.
[Google Scholar](#)
- [Kuroda et al., 2008](#) M. Kuroda, M. Tsujimoto, T. Fujiwara, S. Ohmatsu, K. Takagi
Investigation on components of added resistance in short waves
 J. Jpn. Soc. Nav. Archit. Ocean Eng., 8 (2008), pp. 171-176
[CrossRef](#) [View Record in Scopus](#) [Google Scholar](#)
- [Lee et al., 2013](#) Lee, J.H., Seo, M.G., Park, D.M., Yang, K.K., Kim, K.H., Kim, Y., 2013. Study on the effects of hull form on added resistance. In: Proceeding of the 12th International Symposium on Practical Design of Ships and Other Floating Structures (PRADS2013). Changwon, Korea.
[Google Scholar](#)
- [Liu et al., 2011](#) S. Liu, A. Papanikolaou, G. Zaraphonitis
Prediction of added resistance of ships in waves
 Ocean Eng., 38 (2011), pp. 641-650
[Article](#)  [Download PDF](#) [View Record in Scopus](#) [Google Scholar](#)
- [Mantzaris, 1998](#) D.A. Mantzaris

Rankine Panel Method as a Tool for the Hydrodynamic Design of Complex Marine Vehicle (Ph.D. thesis)

MIT; Cambridge, USA (1998)

[Google Scholar](#)

Maruo, 1960 H. Maruo

The drift of a body floating on waves

J. Ship Res., 4 (3) (1960), pp. 1-10

[View Record in Scopus](#) [Google Scholar](#)

Nakamura and Naito, 1977 S. Nakamura, S. Naito

Propulsive performance of a containership in waves

J. Soc. Nav. Archit. Jpn., 15 (1977), pp. 24-48

[View Record in Scopus](#) [Google Scholar](#)

Nakos, 1990 D.E. Nakos

Ship Wave Patterns and Motions by a Three Dimensional Rankine Panel Method (Ph.D. thesis)

MIT, Cambridge, USA (1990)

[Google Scholar](#)

Newman, 1967 J.N. Newman

The drift force and moment on ships in waves

J. Ship Res., 11 (1967), pp. 51-60

[CrossRef](#) [View Record in Scopus](#) [Google Scholar](#)

Orihara and Miyata, 2003 H. Orihara, H. Miyata

Evaluation of added resistance in regular incident waves by computational fluid dynamics motion simulation using an overlapping grid system

J. Mar. Sci. Technol., 8 (2003), pp. 47-60

[View Record in Scopus](#) [Google Scholar](#)

Sadat-Hosseini et al., 2013 H. Sadat-Hosseini, P. Wu, P.M. Carrica, H. Kim, Y. Toda, F. Stern

CFD verification and validation of added resistance and motions of KVLCC2 with fixed and free surge in short and long head waves

Ocean Eng., 59 (2013), pp. 240-273

[Article](#)  [Download PDF](#) [View Record in Scopus](#) [Google Scholar](#)

Salvesen, 1978 N. Salvesen

Added resistance of ships in waves

J. Hydronaut, 12 (1) (1978), pp. 24-34

[CrossRef](#) [View Record in Scopus](#) [Google Scholar](#)

Seo et al., 2013 M.G. Seo, D.M. Park, K.K. Yang, Y. Kim

Comparative study on computation of ship added resistance in waves

Ocean Eng., 73 (2013), pp. 1-15

[Article](#)  [Download PDF](#) [View Record in Scopus](#) [Google Scholar](#)

Song et al., 2011 M.J. Song, K.H. Kim, Y. Kim

Numerical analysis and validation of weakly nonlinear ship motions and structural loads on modern containership

Ocean Eng., 38 (2011), pp. 77-87

[Article](#)  [Download PDF](#) [View Record in Scopus](#) [Google Scholar](#)

Storm-Tejsen et al., 1973 J. Storm-Tejsen, H.Y.H. Yeh, D.D. Moran

Added resistance in waves

Trans. Soc. Nav. Archit. Mar. Eng., 81 (1973), pp. 250-279

[Google Scholar](#)

Tsujimoto et al., 2008 M. Tsujimoto, K. Shibata, M. Kuroda, K. Takagi

A practical correction method for added resistance in waves

J. Jpn. Soc. Nav. Archit. Ocean Eng., 8 (2008), pp. 141-146

[Google Scholar](#)

Visonneau et al., 2010 Visonneau, M., Queutey, P., Leroyer, A., Deng, G.B., Guilmineau, E., 2010. Ship motions in moderate and steep waves with an interface capturing method. In: Proceedings of the 9th International Conference on Hydrodynamics. Shanghai, China.

[Google Scholar](#)

Waterson and Deconinck, 2007 N.P. Waterson, H. Deconinck

Design principles for bounded higher-order convection schemes – a unified approach

J. Comput. Phys., 224 (2007), pp. 182-207

[Article](#)  [Download PDF](#) [View Record in Scopus](#) [Google Scholar](#)

Xiao et al., 2005 F. Xiao, Y. Honma, T. Kono

A simple algebraic interface capturing scheme using hyperbolic tangent function

Int. J. Numer. Methods Fluids, 48 (2005), pp. 1023-1040

[CrossRef](#) [View Record in Scopus](#) [Google Scholar](#)

Yang et al., 2013 K.K. Yang, B.W. Nam, J.H. Lee, Y. Kim

Numerical analysis of large-amplitude ship motions using FV-based Cartesian grid method

Int. J. Offshore Polar Eng., 23 (3) (2013), pp. 186-196

[View Record in Scopus](#) [Google Scholar](#)

Ye and Hsiung, 1997 H.K. Ye, C.C. Hsiung

Computation of added wave resistance of a restrained floating body in the time-domain

Int. Shipbuild. Prog., 44 (437) (1997), pp. 25-57

[Google Scholar](#)

Yokoi, 2007 K. Yokoi

Efficient implementation of THINC scheme: a simple and practical smoothed VOF algorithm

J. Comput. Phys., 226 (2007), pp. 1985-2002

[Article](#)  [Download PDF](#) [View Record in Scopus](#) [Google Scholar](#)

Zhang et al., 2009 Zhang, S., Weems, K.M., Lin, W.M., 2009. Investigation of the horizontal drifting effects on ships with forward speed. In: Proceedings of the 28th International Conference on Ocean, Offshore and Arctic Engineering. Hawaii, USA.

[Google Scholar](#)

[View Abstract](#)



- About ScienceDirect
- Remote access
- Shopping cart
- Advertise
- Contact and support
- Terms and conditions
- Privacy policy

We use cookies to help provide and enhance our service and tailor content and ads. By continuing you agree to the [use of cookies](#).
Copyright © 2021 Elsevier B.V. or its licensors or contributors. ScienceDirect® is a registered trademark of Elsevier B.V.
ScienceDirect® is a registered trademark of Elsevier B.V.



Typesetting math: 69%

FEEDBACK